ACS Catalysis

Article

Insights into the Oxygen Vacancy Filling Mechanism in CuO/CeO Catalysts: A Key Step Towards High Selectivity in Preferential CO Oxidation

Arantxa Davó-Quiñonero, Esther Bailon-Garcia, Sergio López-Rodríguez, J. Juan-Juan, Dolores Lozano-Castello, Max Garcia-Melchor, Facundo C. Herrera, Eric Pellegrin, Carlos Escudero, and Agustín Bueno-López

ACS Catal., **Just Accepted Manuscript** • DOI: 10.1021/acscatal.0c00648 • Publication Date (Web): 11 May 2020

Insights into the Oxygen Vacancy Filling Mechanism in CuO/CeO_2 Catalysts: A Key Step Towards High Selectivity in Preferential CO Oxidation

Arantxa Davó-Quiñonero[a,b], Esther Bailón-García[a], Sergio López-Rodríguez[a], Jerónimo Juan-Juan[c], Dolores Lozano-Castelló[a], Max García-Melchor[b] , Facundo C. Herrera[d,e], Eric Pellegrin[d,†], Carlos Escudero[d] and Agustín Bueno-López[a*]*

[a]Departamento de Química Inorgánica, Universidad de Alicante, Carretera San Vicente del Raspeig s/n E-03080, Alicante, Spain.

[b]School of Chemistry, CRANN and AMBER Research Centres, Trinity College Dublin, College Green, Dublin 2, Dublin, Ireland.

[c]Servicios Técnicos de Investigación, Universidad de Alicante, Carretera San Vicente del Raspeig s/n E-03080, Alicante, Spain.

[d]ALBA Synchrotron Light Source, Carrer de la Llum 2-26, 08290 Cerdanyola del Vallès, Barcelona, Spain.

[e]Instituto de Investigaciones Fisicoquímicas Teóricas y Aplicadas (INIFTA, CONICET), Departamento de Química, Facultad de Ciencias Exactas, Universidad Nacional de La Plata, Diagonal 113 y 64, 1900 La Plata, Argentina.

KEYWORDS: CO-PROX reaction, ceria, copper, operando NAP–XPS, DFT calculations, oxygen vacancies, reaction mechanism

ABSTRACT: The preferential CO oxidation (CO-PROX) reaction is paramount for the purification of reformate H_2-rich streams, where CuO/CeO_2 catalysts show promising opportunities. This work sheds light on the lattice oxygen recovery mechanism on CuO/CeO_2 catalysts during CO-PROX reaction, which is critical to guarantee both good activity and selectivity, but that is yet to be well understood. Particularly, in situ Raman spectroscopy reveals that oxygen vacancies in the ceria lattice do not form in significant amounts until advanced reaction degrees, whereas pulse O_2 isotopic tests confirm the

involvement of catalyst oxygen in the CO and H_2 oxidation processes occurring at all stages of the CO-PROX reaction (Mars–van Krevelen). Further mechanistic insights are provided by operando near-ambient pressure X-ray photoelectron spectroscopy (NAP–XPS) and near edge X-ray absorption fine structure (NEXAFS) experiments, which prove the gradual CuO reduction and steady oxidized state of Ce ions until the very surface reduction of CeO_2 at the point of selectivity loss. Experiments are complemented by density functional theory (DFT) calculations, which reveal a more facile oxygen refill according to the trend CuO > CeO_2 > Cu_2O. Overall, this work concludes that the oxygen recovery mechanism in CO-PROX switches from a direct mechanism, wherein oxygen restores vacancy sites in the partially reduced CuO particles, to a synergistic mechanism with the participation of ceria once Cu_xO particles reach a critical reduction state. This mechanistic switch ultimately results in a decrease in CO conversion in favor of the undesired H_2 oxidation, which opens-up future research on potential strategies to improve oxygen recovery.

1. Introduction

The preferential CO oxidation (CO-PROX) involves the selective oxidation of the low-content CO impurities (0.5–2% vol.) present in reformate streams after processing in water–gas shift reactors.[1] This catalytic strategy efficiently allows for exhaustive CO removal from H_2-rich streams below the 10-100 ppm CO-tolerance level accepted for proton exchange membrane fuel cells, whose performance and durability are strongly affected by CO poisoning.[2–4] In particular, CO-PROX brings promising opportunities in the implementation of on-board and portable H_2-dependent technologies, where lightness is a requirement.[5]

In the search of active and cost-effective catalysts, copper oxide and cerium oxide binary mixtures have demonstrated noteworthy activity and near-optimal features.[6–9] The catalytic performance of CuO/CeO_2 materials relies on the synergistic metal oxide/support interactions arising from complex redox effects induced between the CuO and CeO_2 phases at the interfacial contact points.[6,10] These redox features include labile electron exchange between the Cu^{2+}/Cu^{+} and Ce^{4+}/Ce^{3+} redox pairs, ease of formation of

surface oxygen vacancies in ceria, and the promotion and stabilization of Cu^+ sites.[11–15] Notably, many precedent studies based on in situ and operando advanced spectroscopic studies have pinpointed the stable surface Cu^+ species as active sites for CO oxidation, whereas the reduced metal Cu entities would favor the undesired H_2 oxidation.[11,16–18] In turn, the oxidation state of copper species is deemed to determine CO selectivity, while the eventual reduction of CuO leads to selectivity losses by virtue of boosting the competing H_2 oxidation at high temperatures.[19–21] Since cationic Cu^+ species are the result of the interfacial redox interactions between the CuO and CeO_2 phases,[22,23] many studies have been devoted to promoting the formation of Cu^+ by means of a rational catalyst nanodesign.[14,15,24–28] Accordingly, highly-dispersed CuO_x particles provide the highest reducibility to copper oxide/cerium oxide mixtures. Conversely, larger CuO_x bulk-like clusters with a weaker interfacial interaction and a kinetically limited interaction help to prevent further reduction to Cu^0 and improve the maintenance of the CO selectivity.[29,30] Therefore, the catalytic performance is influenced by the balance of small $Cu^{\delta+}$ particles

and disperse bulk CuO microstructures, which is tunable by means of catalyst nanodesign controlling size, shape, composition and electronic effects.

Recent studies based on advanced in situ transient techniques have presented valuable mechanistic insights in the copper-catalyzed CO-PROX reaction[31–33] and it is a general consensus that reaction takes place mainly following a Mars–van Krevelen (MvK) mechanism.[32,34,35] Since MvK mechanism involves the direct participation of lattice oxygen species in the reaction, oxygen vacancies created in the neighborhood of active sites, which must be replenished by molecular O_2 from the gas phase. Thus, the catalyst reoxidation capacity given by the surface oxygen exchange ability and oxygen mobility has a direct impact in the catalytic performance.[36,37] However, in contrast with the current deep knowledge in molecular CO and H_2 oxidation reactions, the mechanism of reoxidation steps is not yet well understood.[32,38,39] In copper oxide–cerium oxide catalysts, two complementary mechanisms of O vacancy filling have been proposed. Namely, the *direct* mechanism where O_2 replenishes oxygen vacancies directly in the CuO_x sites, and the *synergistic* mechanism, where O_2 uptake takes place via the CeO_2

support and subsequent transfer to the active O-deficient CuO_x phase.[40] Although the prevalence of each mechanism is known to be dependent on the oxygen storage capacity and catalyst interfacial interactions, the assessment of their specific contributions during CO-PROX conditions remains unclear.

Herein we report a detailed mechanistic insight on the CuO/CeO_2 activity towards the CO-PROX reaction with a particular focus on the redox processes occurring at the individual catalytic phases in reduction and reoxidation steps. With this aim, CO-PROX operando near-ambient pressure X-ray photoelectronic spectroscopy (NAP–XPS) and near edge X-ray absorption fine structure (NEXAFS) experiments with tunable incident soft X-ray photon energies were conducted, obtaining XPS spectra which allow to discern with high sensitivity small variations in the redox processes at different catalyst depths. Particularly, while Cu ions are gradually reduced along with CO-PROX reaction course, Ce ions remain in a steady oxidized state up to a critical point where the finest surface of ceria shows an incipient reduction. In addition, DFT calculations indicate that ceria facilitates oxygen to the surrounding Cu species at the triple phase boundary, assisting in the

oxygen recovery process once Cu reaches a certain reduced state. In situ Raman spectroscopy in CO-PROX mixture confirms that ceria reduction becomes very significant when further increasing the temperature above such point, assigned to the total conversion of inlet O_2. On the contrary, O_2 pulse isotopic experiments demonstrate the involvement of catalyst oxygen in the CO and H_2 oxidations along the entire CO-PROX reaction range, which overall suggests the participation of lattice oxygen from different sources, from CuO in first instance, and secondly, from ceria. In summary, this work presents evidences of the transition from a direct O vacancy filling mechanism on CuO, to a synergistic O_2 uptake via ceria, which determines the CO-PROX selectivity of the CuO/CeO_2 catalyst.

2. Experimental methods

2.1. Catalysts preparation and characterization

The CeO_2 support was prepared by thermal decomposition of cerium(III) nitrate following *flash* calcination procedure, introducing the precursor in a preheated muffle furnace at 200 ºC and then heating up to 500 ºC in a ramp of 10 ºC/min. The CuO/CeO_2 catalyst

was synthesized via incipient wetness impregnation of copper(II) nitrate aqueous solution into the ceria support, followed by *flash* calcination with the same protocol as for the support preparation. The target nominal composition was set to 5% w/w Cu.

The general physicochemical characterization results, including N_2 adsorption at –196 ºC (Figure S1, Table S1), XRD (Figure S2, Table S2), Raman spectroscopy (Figure S3), temperature programmed reduction with H_2 (Figure S4) and transmission electron microscopy (Figure S5), are described in the Supporting Information.

2.2. CO-PROX catalytic tests

Fixed-bed CO-PROX catalytic tests were conducted with 150 mg of catalyst placed in a U-shaped quartz reactor (16 mm inner diameter) and 100 mL/min (GHSV: 30000 h^{-1}) of the flowing reactant mixture, i.e., 2% CO, 30% H_2 and 2% O_2 balance N_2, leading to a stoichiometric O_2:CO excess (λ) of 2. To test the effect of the oxygen partial pressure, experiments in O_2:CO stoichiometric conditions with $\lambda = 1$ were also carried out. Catalytic tests were performed with a heating rate of 2 ºC/min up to 250 ºC and the exhaust gases were analyzed using a gas chromatograph (HP model 6890 Plus Series) equipped with

two columns: Porapak Q 80/100 for CO_2 and H_2O separation and Molecular Sieve 13X for O_2 and CO separation, coupled to a thermal conductivity detector (TCD). The effect of CO_2 and H_2O inhibitors in the catalytic activity was studied by adding 10% CO_2, 5% H_2O and 10% CO_2 + 5% H_2O to the reactant CO-PROX gas mixture in 2 ºC/min ramp experiments with λ = 2 (Figure S9).

2.3. Isotopic experiments with $^{36}O_2$

Isotopic experiments were performed with $^{36}O_2$ using an injection valve with a loop (100 µL) and two high sensitivity pressure transducers. These experiments were carried out in a fixed-bed tubular quartz reactor with 80 mg of catalyst in a constant feeding mixture consisting of 20 mL/min of 1% CO, 30% H_2 and He balance. The outlet gas composition was monitored with a mass spectrometer (MS) Pfeiffer Vacuum (model OmniStar). The reactor was heated using a furnace controlled by a temperature regulator at selected temperatures representative for different CO selectivity regimes along the CO-PROX reaction, namely 75, 100 and 150 ºC. Once MS signals were stabilized at the desired temperature under the flowing mixture, three $^{36}O_2$ pulses (Isotec, 99%; 100 µL and 620

mbar) were injected. The results obtained were reproducible at all temperatures, and the reproducibility of the method was further confirmed by the injection of Ar pulses (100 µL and 620 mbar) prior to the $^{36}O_2$ pulses.

2.4. In situ Raman spectroscopy experiments

In situ Raman spectra were recorded in a LabRam Jobin Ivon Horiba instrument with a laser excitation source of He:Ne (632.8 nm). Experiments were performed in a high temperature chamber fed with a regular flow of 100 mL/min of He or CO-PROX gas mixture (i.e., 2% CO, 2% O_2, 30% H_2 and He balance). Raman spectra were recorded in both atmospheres at selected temperatures (i.e., 50, 75, 100, 150, 200 and 250 ºC) to study structural changes upon exposure to the CO-PROX reactant mixture. A monocrystalline Si reference (521 cm^{-1}) was used to calibrate the position of the bands.

2.5. NAP–XPS and NEXAFS experiments under CO-PROX operando conditions

NAP–XPS spectra were recorded under CO-PROX reaction conditions at the NAPP branch of the CIRCE beamline at the ALBA Synchrotron Light Source.[41] For each analysis, two different set of photon energies were used, namely 1082 and 1372 eV for

the Ce 3d and Cu 2p regions, and 972 and 722 eV for the O 1s and C 1s regions. These energies provide a variability in the surface sensitivity according to the estimations of the mean free paths (MFP) in the Cu and Ce oxide structures (see Table S3 for details). The CuO/CeO_2 catalyst was pelletized with a gold mesh to prevent surface charging while providing a Au 4f reference for the peak position during XPS analysis. Catalytic activity of the gold mesh was experimentally ruled out. A Puregas gas inlet system (SPECS) was used to keep the total pressure in the XPS chamber constant at 1 mbar and to control the gas feed. The pelletized catalyst was pretreated in O_2/He atmosphere at 250 ºC for 1 hour and then cooled down to 50 ºC. Subsequently, the CO-PROX reacting mixture containing 1% CO, 1% O_2, 30% H_2 and balance N_2 was dosed at 30 mL/min, and exhaust gases were monitored with a MS installed in the second stage of the differential pumping system of the XPS electron energy analyzer. The CO-PROX reaction progress was controlled at temperature intervals of 50 ºC with corresponding stabilization at each point up to total O_2 conversion until reaching the final temperature of 450 ºC. For each temperature, XPS

spectra were recorded once stationary state was achieved based on MS signals stabilization.

CO-PROX operando NEXAFS measurements at the Cu L-edge (930-950 eV) were performed in total electron yield mode measuring the sample current at each temperature after the series of NAP–XPS scans using the same experimental conditions.

2.6. Computational methods

Theoretical calculations reported in this work were conducted by means of periodic density functional theory (DFT) using the Perdew-Burke-Ernzenhof (PBE) exchange-correlation functional,[42] as implemented in the Vienna ab initio simulation package (VASP) code, version 5.4.1.[43,44] The core electrons of Ce, Cu and O ions were described using projector augmented wave (PAW) potentials,[45] while their valence states were represented by plane-waves with a kinetic cut-off energy of 500 eV. In the case of Ce ions, an effective Hubbard U term (U_{eff}) of 4.5 eV was also added to the DFT calculated energies (DFT+U) as an on-site correction for the electrons localized in the 4f orbital, following Dudarev's approach.[46] The choice of this U_{eff} value is based on the satisfactory

results obtained for a wide range of reactions catalyzed by ceria.[47–50] In the case of Cu^{2+}, the analogue treatment of the d^9 electron was conducted using an U_{eff} of 7, as recommended in literature.[51]

The equilibrium lattice constant for the Cu and Ce bulk oxides was optimized with a Γ-centered k-point grid of 5 □ 5 □ 5 and 7 □ 7 □ 7, respectively, and using the Birch-Murnaghan equation of state. Starting from the optimized bulk structures, the most abundant facets were modelled by their corresponding surface slabs, namely CuO(111), Cu_2O(111) and CeO_2 (111) displaying different periodicities in order to expose equal number of surface oxygens. These slabs were built thick enough to ensure there is minimal interaction between the top and the bottom (3 metal layers for CeO_2, 4 for CuO and Cu_2O slabs), and with a sufficiently large vacuum gap (ca. 15 Å) perpendicular to the surface to minimize the interaction between periodic slabs in that direction. The geometry of the surface slabs was optimized using a Γ-centered k-point grid mesh of 3 □ 3 □ 1. Oxygen vacancy formation energies, $E_{O\text{-}vac}$, on the various slabs were calculated as:

$$E_{O\text{-}vac} = E_{vac\text{-}slab} - [E_{slab} + ½\, E_{O2}]$$

Where E_{slab} is the energy of the stoichiometric slab, E_{O2} is the energy of an oxygen gas molecule, and $E_{vac\text{-}slab}$ is the energy of the slab with a lattice oxygen vacancy with the two electrons left behind in the most favorable configuration. All the $E_{O\text{-}vac}$ values featuring different electron distributions are presented in Table S4.

3. Results and discussion

3.1. CO-PROX catalytic tests in fixed-bed reactor

Figure 1 shows the CO-PROX activity profile of the prepared CuO/CeO_2 catalyst in a first reaction cycle at two different oxygen partial pressures. Regardless the oxygen inlet, CuO/CeO_2 exhibits an exceptional behavior in terms of CO conversion and CO selectivity, in agreement with previous studies.[52–54] Because of the competitive H_2 oxidation reaction, two different regions must be discerned in Figure 1, namely the CO selective (ca. <110 ºC) and non-selective regime (ca. >110 ºC). Such critical temperature is defined by the H_2 oxidation onset, process which becomes more predominant as temperature increases because of its higher activation energy compared to CO oxidation.[55] In consequence, the selectivity regime transition is relevant since it dictates the optimum operating

temperature in for the optimum CO activity and selectivity for a given experimental CO-PROX reaction conditions. According to Figures 1a and 1b, neither CO oxidation nor H_2 oxidation onset are significantly affected by the inlet O_2 pressure as the transition between both regimes remains unaltered.

However, as H_2 gains relevance, CO oxidation is hampered due to the limited O_2 supply, as illustrated in the selectivity profile. When X_{O2} is total, CO conversion decreases in favor of H_2 oxidation, which occurs near the regime transition point in λ=1 conditions, while at higher temperatures when λ=2. Besides, the O_2:CO excess (λ=2) allows to reach higher CO conversions compared to the stoichiometric conditions (λ=1) since H_2 oxidation onset is lower than the temperature required for total X_{CO}. Hence, setting λ>1 is beneficial in CO-PROX, though only moderate values are practicable in order to avoid an excessive residual H_2 oxidation.[56,57] Therefore λ=2 will be set as the default CO-PROX conditions for the operando analyses presented henceforward in this study. Overall, these results confirm that CO-PROX is a competitive process where selectivity is determined by the

remaining partial pressure of O_2, although CO and H_2 oxidation reactions are not affected independently.

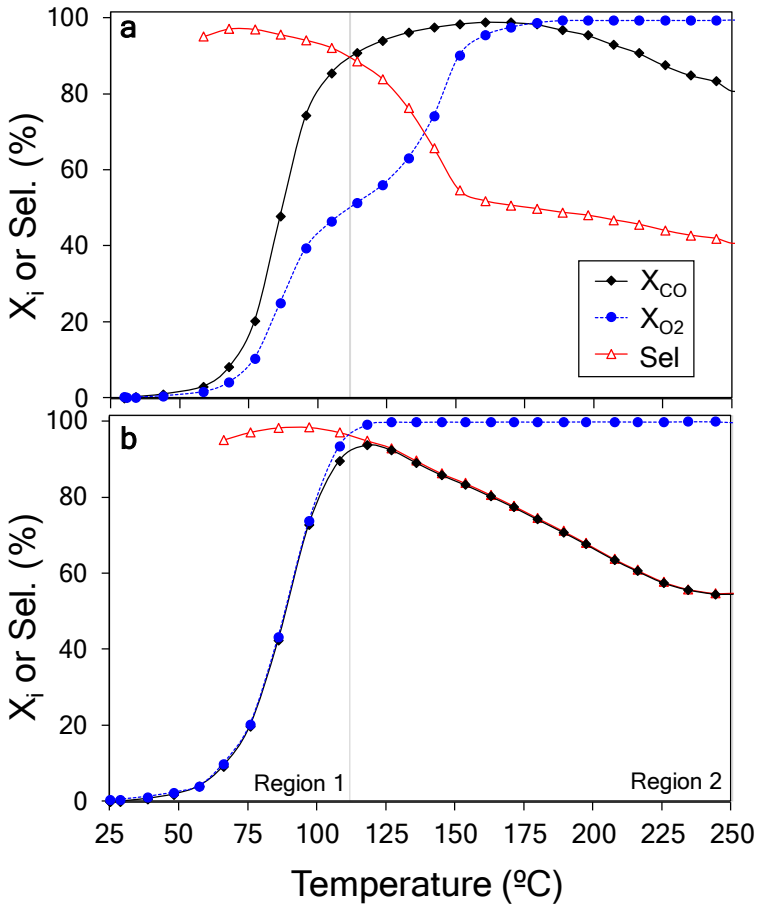

Figure 1. CO-PROX catalytic performance of CuO/CeO_2 in terms of CO conversion (X_{CO}, diamonds), O_2 conversion (X_{O2}, circles), and CO selectivity (*Sel*, triangles) profiles for a) λ=2 and b) λ=1. Region 1 refers to the CO selective regime, whereas Region 2 corresponds to the non-selective regime.

Catalytic tests using the CeO_2 and CuO bare phases were carried out as control experiments and both showed negligible individual activity within the CO-PROX temperature window (Figure S6) in contrast to the binary CuO/CeO_2 catalyst. These experiments point out to the synergistic Cu–Ce interactions at the CuO/CeO_2 interface as the main responsible for the improved performance of the combined catalyst, as well reported.[27,28,58,59] In this regard, characterization by Raman spectroscopy (Figure S3) and H_2-TPR (Figure S4) prove the existing strong interaction between CuO and CeO_2 in the CuO/CeO_2 catalyst. Altogether, the general characterization results indicate that the 5% w/w Cu catalyst prepared by *flash* calcination is composed of both finely disperse CuO_x particles and bigger CuO bulk-like clusters in weaker interaction with the ceria carrier. A minor portion of 0.56% Cu is estimated to be inserted in the ceria lattice (Table S2), presumably concentrated on the outer surface layers.

The robustness and recyclability of the CuO/CeO_2 catalyst was confirmed by running four consecutive CO-PROX reaction cycles (Figure S7) followed by a fifth 10 hours' time-on-stream isothermal experiment (Figure S8). Finally, the suitability of the CuO/CeO_2 catalyst

in the presence of CO_2 and H_2O inhibitors was demonstrated, whose resulting impact in the catalytic activity followed the trend: CO_2 < H_2O < CO_2 + H_2O (see Figure S9), in agreement with previous studies. [57,60] Overall, the CO-PROX activity results demonstrate excellent performance of the CuO/CeO_2 catalyst.

3.2. $^{36}O_2$ pulse isotopic experiments

To investigate the participation of lattice oxygen from the CuO/CeO_2 catalyst in the CO-PROX reaction mechanism, a series of $^{36}O_2$ pulse isotopic experiments were next performed at different temperatures. According to the gas profiles measured after the $^{36}O_2$ pulses (Figure 2), only CO_2 and H_2O species were detected with no sign of O_2 being released. This observation can be rationalized with the strongly reducing conditions of these experiments, leading to a highly O-deficient CuO/CeO_2 catalyst that captures the incoming $^{36}O_2$ molecules to restore the O vacant sites. In addition, Figure 2 shows that the area of the $^{18}H_2O$ peak increases with temperature due to the promoted H_2 oxidation reaction, while the area of the CO_2 peaks decreases due to the selectivity loss in the CO-PROX reaction (Figure S10), in agreement with the catalytic experiments described in the

previous section. The effect of the temperature is also reflected in the sharpening of the profiles of the evolved products, which can be attributed to a faster desorption. The most relevant insight, however, is the evident delay in H_2O release compared to CO_2, as well as the large broadening of the H_2O signal. This is consistent with an increased retention of water molecules at the surface compared to CO_2. The potential accumulation of H_2O on the catalyst surface also relates with the stronger inhibition by H_2O than by CO_2, as the corresponding catalytic results show (Figure S9).[57,60] In addition, complementary temperature programmed experiments (TPD) from Figure S10 in the Supplementary Information evidence a significant H_2O and CO_2 retention capacity in the CuO/CeO_2 catalyst. Interestingly, H_2O surface saturation leads to important CO_2 co-release, and vice versa. In fact, CO_2 and H_2O co-addition maximizes chemisorption capacity, which also relates with the much stronger inhibition by CO_2 + H_2O co-presence (Figure S9).

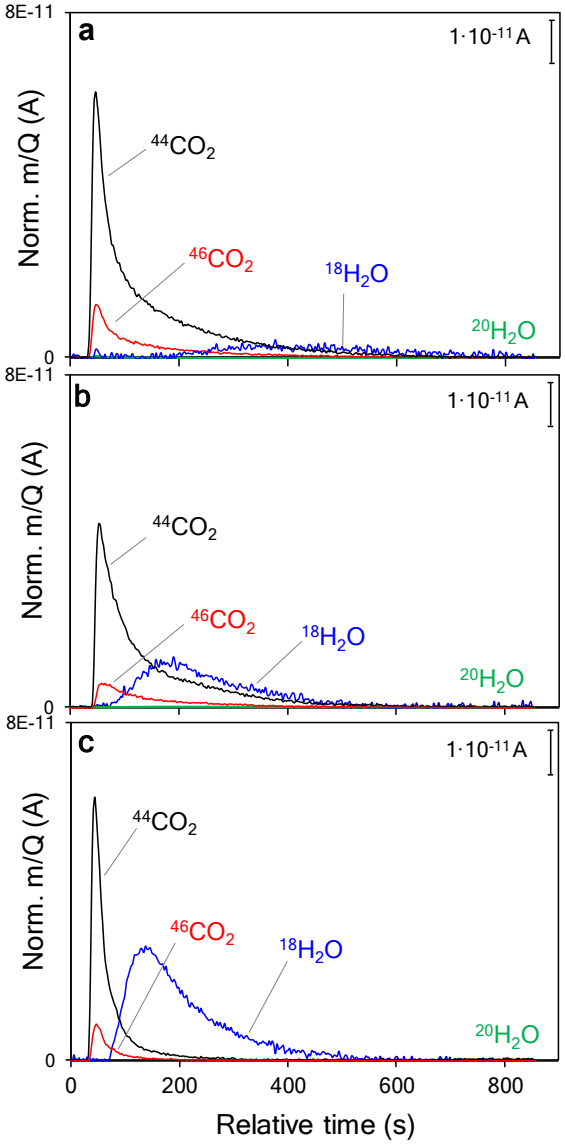

Figure 2. Normalized MS signals measured after $^{36}O_2$ pulses in H_2 + CO flow with the CuO/CeO_2 catalyst at different temperatures: a) 75 ºC, b) 100 ºC and c) 150 ºC. The zero-time was set after $^{36}O_2$ was pulsed.

The signals detected after the $^{36}O_2$ pulses correspond to $^{44}CO_2$, $^{46}CO_2$ and $^{18}H_2O$, where most oxygen atoms come from CO and the catalyst O atoms (^{16}O); the only ^{18}O-containing molecule was $^{46}CO_2$, and neither $^{48}CO_2$ nor $^{20}H_2O$ were detected. Notably, the formation of $^{44}CO_2$ ($^{16}OC^{16}O$; non-isotopic) involves catalyst ^{16}O abstraction and anionic vacancy formation, which is indicative of CO oxidation taking place via a Mars–van Krevelen (MvK) mechanism. On the other hand, $^{46}CO_2$ formation ($^{18}OC^{16}O$; scramble of non-isotopic and isotopic) may involve an adsorbed ^{18}O species in the vicinity of CO or occur via direct oxidation of adsorbed CO by $^{36}O_2$. The relative areas of the $^{44}CO_2$ and $^{46}CO_2$ peaks, however, indicate that the former reaction pathway is much more relevant than the latter regardless of the temperature. Analogously, H_2 oxidation involves a catalyst oxygen (^{16}O) to yield $^{18}H_2O$ via a MvK mechanism. In contrast with CO oxidation, other alternative H_2 oxidation mechanisms involving pulsed $^{36}O_2$ can be ruled out since $^{20}H_2O$ is not detected. In summary, isotopic pulse experiments allow to unequivocally confirm that both CO and H_2 oxidation reactions on the CuO/CeO_2 catalyst in a CO-PROX environment occur via a MvK mechanism all along the temperature profile. Besides,

global isotopic yield of products shown in Figure S11 demonstrate there is not significant effect of temperature in the oxygen exchange capacity of the catalyst within the 75–150 ºC tested range.

3.3. In situ Raman spectroscopy experiments

Figure 3 compiles the Raman spectra of the CuO/CeO_2 catalyst recorded under flowing He and CO-PROX gas mixture atmospheres at different temperatures, which relate with ceria crystalline changes. The spectra show a main band centered around 464 cm^{-1}, attributed to the F_{2g} symmetric vibration mode of oxide anions around their equilibrium positions in tetrahedral sites within the cubic crystal structure of ceria.[7,61,62] The position of the F_{2g} band is highly sensitive to small changes in the crystalline features of CeO_2 and it is well reported to respond upon lattice dilation with a proportional lower frequency (red) shift.[62] Additionally, Raman spectra of ceria-based materials typically display minor bands around 540 cm^{-1} and 600 cm^{-1}, so-called D bands, D_1 and D_2 respectively, which are ascribed to the presence of lattice defects.[61,63] Hence, the area band ratio D/F_{2g} is widely used a measure of oxygen defect concentration in ceria, though the discernment between

the D_1 and D_2 band modes is still a matter of debate.[64] Recent experimental/computational Raman studies in ceria-doped materials have assigned D_1 bands to the presence of oxygen vacancy defects, whereas D_2 is attributed to the presence of defective elements in solid solution within the ceria crystal.[63–65]

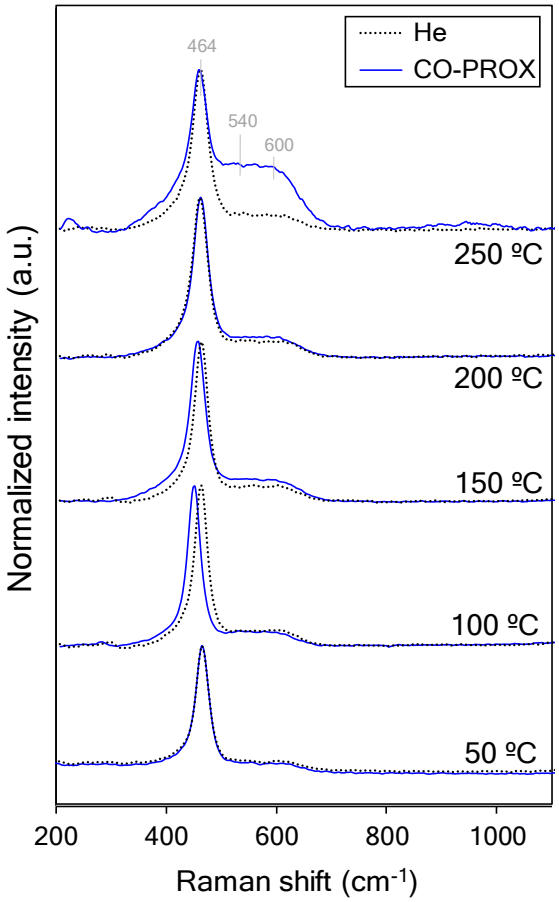

Figure 3. In situ Raman spectra for the CuO/CeO_2 catalyst recorded at different temperatures in 100 mL/min of He (dotted lines) and CO-PROX mixture (solid lines). We note that spectra have been normalized to the maximum intensity of the F_{2g} band.

Since pulse isotopic experiments confirm a MvK mechanism in CO-PROX for both CO and H_2 oxidation reactions, it is expected an increased population of oxygen vacancies in the catalyst alongside reaction course. The formation of an O vacancy results in a charge imbalance in the CeO_2 lattice that must be compensated by the reduction of two Ce^{4+} cations to Ce^{3+}. The distribution of the reduced Ce^{3+} ions is determined by the most favorable arrangement around the vacancy site, which has been established as the nearest neighbor (*NN*) and next nearest neighbor (*NNN*) positions relative to the defect position.[66] As a result, the Ce^{3+}–*NNN* cation formed upon oxygen vacancy formation would remain in an 8-fold coordination contributing to the D_2 mode, as a sign of incipient reduction of ceria with highly dispersed surface oxygen vacancies. Assuming this hypothesis, the D_2 band at 600 cm^{-1} attributed to isolated vacancies, cannot be formed in independence of the D_1 band at 540 cm^{-1} in non-doped ceria materials, as is the case of

this study. For this reason, the in situ Raman spectra presented herein show near-equal D_1 and D_2 contributions, which are gathered together as a broad D band that acquires a flat profile in the 540-600 cm^{-1} range. The influence of temperature on the D and F_{2g} Raman bands in He and CO-PROX atmospheres is compiled in Figures 4a and 4b.

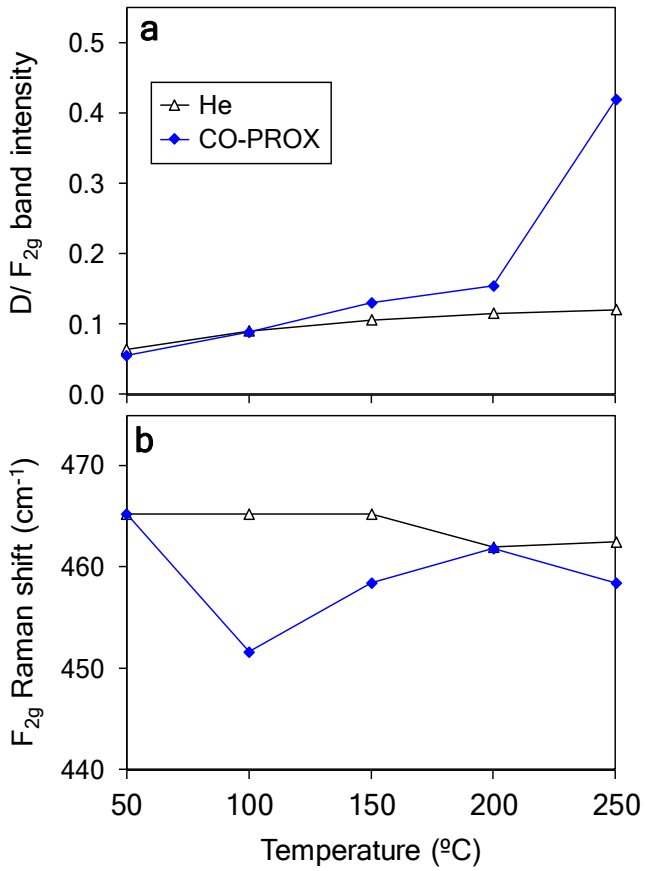

Figure 4. Data extracted from Raman spectra at different temperatures in He (triangles) and CO-PROX (diamonds) conditions. a) D (540–600 cm^{-1}) / F_{2g} (460 cm^{-1}) band intensity ratios and b) F_{2g} band Raman shift.

The comparison between the trends observed under He and CO-PROX conditions allows to discern the effect of reactant gases from the inherent lattice thermal expansion in the CuO/CeO_2 catalyst. According to the He-recorded Raman spectra shown in Figure 3, the ceria lattice is expanded by the effect of temperature above 150 ºC resulting in a proportional F_{2g} red shift. Another contribution to such expansion is the presence of Ce^{3+} cations, with larger radii than Ce^{4+}, that balance the charge deficit left upon the formation of oxygen vacancies in ceria induced by temperature. However, the associated defect D band barely increases within 50–250 ºC, so this contribution is modest.

On the other hand, the recorded CO-PROX Raman spectra is more complex and responds to the different CO-PROX reaction regimes. In particular, the evolution of the D band in the CO-PROX mixture (Figure 4a) encompasses that recorded in He up to 100 ºC. Beyond this temperature, the CuO/CeO_2 catalyst presents a gradually higher

population of oxygen vacancy defects under CO-PROX conditions, which experiences a sharp increase at 250 ºC. Considering that the Raman spectra for CuO/CeO_2 merely relate to the crystalline properties of ceria since the CuO Raman bands are weak,[67] we can conclude that ceria remains essentially oxidized below 100 ºC. After this temperature, there is a moderate reduction of ceria under CO-PROX conditions up to 200 ºC, after which a critically reduced state is suddenly observed. This is in agreement with the fixed-bed catalytic tests (Figure 1) and O_2 isotopic pulse experiments (Figure 2) which suggest that the MvK mechanism is eventually disrupted in low O_2 partial pressure conditions when H_2 oxidation becomes more relevant, and consequently, CO selectivity drops.

Interestingly, the analysis of the F_{2g} band presented in Figure 4b and its comparison with the evolution of the D band leads to the striking observation that lattice expansion and oxygen vacancy formation are not coupled along the CO-PROX reaction. For instance, at 100 ºC, the F_{2g} band exhibits a large red shift that is not encompassed by an increase of the D band. One possible explanation could be that oxygen vacancies created upon the reduction of Ce^{4+} ions by CO are rapidly refilled by O atoms from O_2, forming transient

surface oxygen species that do not transfer negative charge density to the neighboring Ce^{3+} cations, which remain reduced. This scenario typically entails reactive oxygen species such as peroxides (O_2^{2-}) and superoxides (O^{2-}) that are characterized by the presence of weak bands centered at 830 and 1130 cm^{-1}, respectively.[68,69] However, these bands were not detected in the CO-PROX Raman spectra, and therefore, the participation of these oxygen species is questionable. Besides, this hypothesis would involve a major contribution from the D_2 component in the D band region, which could not be observed either. An alternative and more likely explanation is that the chemisorption of H_2 and subsequent surface hydroxylation may lead to the reduction of Ce^{4+} ions at these low temperatures, where lattice oxygen abstraction by water release is still not favorable. This possibility is supported by previous experimental and theoretical studies which show that the dissociative H_2 chemisorption can indeed promote the reduction of surface Ce^{4+} ions leaving a large coverage of Ce^{3+}–OH groups.[49,70] The low energy activated H would remain on surface as hydroxyl groups or reversibly recombine to release back H_2 unless sufficient energy is provided by higher temperatures to produce

water molecules at expense of the formation of an O vacancy. In turn, under H_2 atmosphere and low temperatures (ca. <100 ºC), CeO_2 surface presents one-electron (i.e., punctual Ce^{3+} sites) formed upon a reversible process not related to oxygen vacancy formation. However, the magnitude of the red-shift of the F_{2g} band suggests that there may be other factors at play at these low temperatures. Another unexpected observation arises at higher temperatures, where the F_{2g} band shows a gradual compression of the ceria until it overlaps with the He-recorded spectrum at 200 ºC. Finally, the F_{2g} red-shift at 250 ºC is accompanied by a steep increase of the D band (Figure 4a), which indicates that ceria lattice expansion is directly related to oxygen vacancy formation at this temperature, as one would expect.

Overall, the Raman spectra presented in Figure 4 prove the existence of dynamic redox processes in ceria under CO-PROX reaction conditions, which cannot be explained without the knowledge of the state of Cu particles in the combined CuO/CeO_2 catalyst.

3.5. CO-PROX operando NAP–XPS and NEXAFS experiments

CO-PROX conditions using the CuO/CeO_2 catalyst were reproduced in a NAP–XPS analysis chamber, and the XPS spectra were recorded at different temperatures up to 100% O_2 conversion. Before these experiments, spectra were also recorded during the oxidizing pretreatment in O_2/N_2 at 200 ºC, as an indicator of the initial oxidation state of the catalyst. The O_2 conversion profile obtained in the NAP–XPS experiments is presented in Figure 5 along with the profile obtained in the fixed-bed reactor (Figure 1a) for comparison. The CO-PROX spectrum recorded at 50 ºC does not show good resolution because of the moderate conductivity of the sample at this low temperature, which resulted in severe surface charging and eventually difficult deconvolution fitting due to the broadening of the peaks. We also note that the observed catalytic activity dependence with temperature is very different in the operando NAP–XPS experiment when compared to the fixed-bed reactor (Figure 5). Notably, much higher temperatures were needed in the CO-PROX operando NAP–XPS experiment to achieve total O_2 consumption.

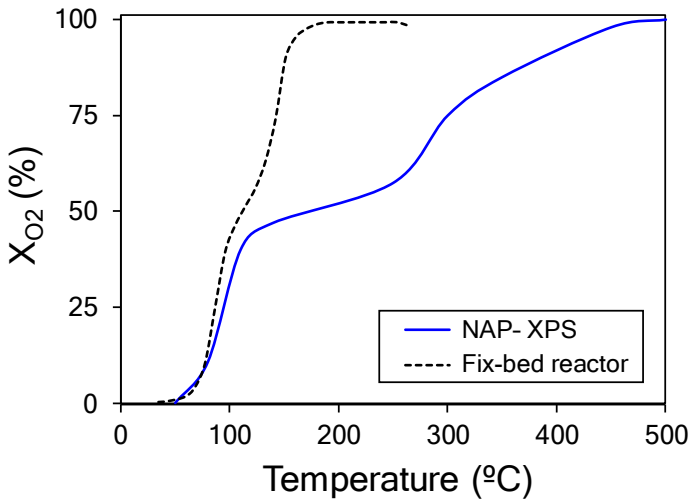

Figure 5. O_2 conversion (X_{O2}) profiles as a function of temperature for the CuO/CeO_2 catalyst under CO-PROX reaction conditions (with $\lambda = 2$): 100 mL/min, 1 bar in the fixed-bed reactor tests (dashed line), and 30 mL/min, 1 mbar in the NAP–XPS experiment (solid line).

As previously described, the double S-shaped curve observed in Figure 5 is a consequence of the separate onsets for CO and H_2 oxidation reactions and the chosen stoichiometric O_2:CO excess of $\lambda = 2$. However, in the case of the NAP–XPS experiment, the onset for H_2 oxidation is much more delayed probably due to the large difference in the total working pressure and measurement conditions, which causes the CO oxidation to remain selective for a wider temperature window. The C 1s and O 1s XPS regions

recorded at 722 eV (Figure S13) reveal surface chemistry changes in the CuO/CeO_2 catalyst rather than redox processes directly involved in the CO-PROX mechanism. Briefly, the high binding energy O contribution (ca. 531.5 eV) in O 1s XPS region assigned to loosely bound O surface species was found to gain considerable importance, while carbonaceous species coverage (C 1s XPS signal) tend to disappear. This observation can be related with the hypothesized H_2O accumulation predicted by the delay in H_2O release during isotopic experiments, and at the same time, to the shift in H_2 oxidation onset seen in the NAP–XPS experiments. However, standalone analysis of C 1s and O 1s XPS spectra cannot provide conclusive insights in this regard. Conversely, the proper catalyst surface analysis under CO-PROX conditions by means of operando DRIFTS–MS experiments reveals hydroxyl depletion rather than accumulation (see Figure S12). Furthermore, it has been reported a relation between hydroxyl consumption and bicarbonate-type intermediates formation,[52] which results positive to favor the desorption of C-species (bicarbonates compared to carbonates). Therefore, hydroxyl groups arising presumably from the low-temperature H_2 activation on the copper and cerium oxides

phases turn out to be beneficial for the CO oxidation reaction kinetics.[71] The effect of H_2 is only positive below the H_2 oxidation reaction onset, point above which OH groups would be instead released form water via MvK mechanism, in a process competing with CO oxidation. Noticeably, taking into account the important pressure difference between the NAP–XPS and DRIFTS analysis chambers (i.e., 0.001 bar vs 1 bar) it should be considered that the surface chemistry might present different behaviors in terms of hydroxyl and C-species coverage. Alternatively, O_γ peak can be attributed to weakly-bounded surface O species present in an O-defective CeO_2 surface, e.g., peroxide or superoxide reactive species. However, since the assignation of O_γ is ambiguous, we cannot confirm neither rule out any of both explanations.

The Ce 3d and Cu 2p XPS regions were scanned using two different photon energies: 1082 and 1372 eV (E_1 and E_2, respectively) to probe different surface depths in the CuO/CeO_2 catalyst according to inelastic mean free path (IMFP) calculations,[72–75] as presented in Table S3 for Cu and Ce oxides. While differences in depth are moderate (ca. 4 Å), it is well-known that the lower the X-ray energy, the lower the IMFP, and

therefore, the probing depth. The XPS spectra recorded at 1082 eV are illustrated in Figures 6a-b, whereas the main results obtained with both energies are summarized in Table 1.

Figure 6a shows the deconvoluted Ce 3d XPS region (taken at 1082 eV) for the CuO/CeO_2 catalyst under different conditions and the fitting assignment based on the standard nomenclature provided by Burroughs et al.[76] Results of the estimated Ce^{3+} content[77–79]obtained from the spectra taken at 1082 and 1372 eV for the CuO/CeO_2 catalyst are presented in Table 1. According to these data, the Ce^{3+} content remains constant at around 20% until 450 ºC, where partial reduction of ceria occurs, increasing Ce^{3+} up to 33%. Comparing both incident X-ray energies, we also observe that the lower energy allows to discern much better the partial reduction of ceria, which highlights the very superficial degree of the reduction as the target depth difference between both energies is within 4 Å (see Table S3).

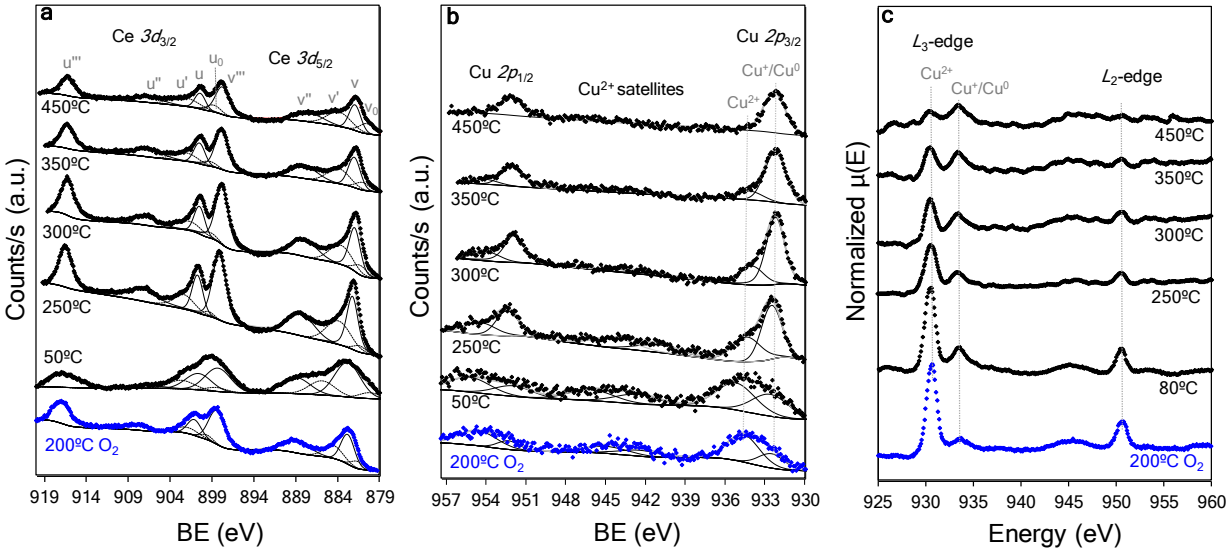

Figure 6. a) Ce 3d and b) Cu 2p XPS region analyses of the CuO/CeO_2 catalyst in O_2 (blue) and CO-PROX reaction conditions (black) at different temperatures taken at 1082 eV photon energy. Dotted lines in Figure 6a correspond to the contribution of Ce^{3+} species. c) Normalized Cu L-edge NEXAFS spectra of the CuO/CeO_2 catalyst under different experimental conditions.

The Cu 2p XPS spectra presented in Figure 6b show the Cu $2p_{3/2}$ and Cu $2p_{1/2}$ peaks and the well-reported shake-up satellite characteristic of the presence of Cu^{2+} ions.[80,81] Each of the Cu 2p peaks could be theoretically deconvoluted into three components, which can be attributed to Cu^0, Cu^+ and Cu^{2+} contributions.[82,83] Unfortunately, the statistical

separation between the peak contributions from Cu^0 and Cu^+ is too small to discern between both reduced states. For this reason, we opted to perform a two-peak fitting using precise constraints on BE, FWHM and peak-shape parameters, as representative for oxidized copper (CuO) and the undistinguishable reduced copper species (Cu and Cu_2O)

Table 1. Semi-quantitative determination from the Ce 3d and Cu 2p XPS spectra and Cu L-edge XAS data from the NEXAFS analysis.

Conditions	XPS Ce^{3+} (%)		XPS Cu^{2+} (%)		Cu^{2+}(%) NEXAFS
	E_1	E_2	E_1	E_2	
O_2 200 ºC	20	22	66	75	88
CO-PROX, 50ºC	21	18	58	57	80
250 ºC	22	18	38	37	76
300 ºC	22	19	30	28	66
350 ºC	24	20	21	20	58
450 ºC	33	24	0	0	40

Note: E_1 and E_2 stand for 1082 and 1372 eV incident energies, respectively.

The semi-quantitative estimation of the average oxidation state of surface copper species is presented in Table 1. According to our data, copper is gradually reduced under CO-PROX conditions until reaching a total reduced state (Cu^{+} and/or Cu^{0}) at the highest temperature, with no significant difference between the two X-ray energies employed. Interestingly, even in O_2 atmosphere during the initial oxidation pretreatment, a significant Cu^{+} contribution is observed, which can be attributed to a promoted reduction arising from the redox interplay between the Ce^{4+}/Ce^{3+} and Cu^{2+}/Cu^{+} ions. In this case, however, evident discrepancies were observed in the O_2/N_2 mixture with the 1082 (E_1) and 1372 eV (E_2) photon energies, being Cu noticeably more reduced in the most external profile. We acknowledge that the presence of that large amount of reduced Cu in the CuO/CeO_2 catalyst is very questionable in such oxidizing conditions, even considering the well-known facile oxidation of copper. Consequently, we ascribe those differences to Cu–Ce synergistic interactions and a labile Cu^{2+}/Cu^{+} equilibrium upon Ce^{4+}/Ce^{3+} redox exchange at the most external interfacial layers.

To complement the NAP–XPS characterization during CO-PROX, we next set out to measure the Cu *L*-edge NEXAFS spectra of the CuO/CeO_2 catalyst under different experimental conditions. These spectra are presented in Figure 6c and feature the L_3 and L_2 absorption peaks centered at ca. 930 and 950 eV, respectively, which correspond to the electric dipole allowed $2p \rightarrow 3d$ transition.[84,85] The *L*-edge spectrum for the CuO/CeO_2 catalyst is composed of proportional contributions of characteristic spectral features from CuO, Cu_2O and Cu. Particularly, both CuO and Cu_2O have well-resolved strong L_3 absorption edges, which were assigned to the peaks centered at 930.8 and 933.7 eV, respectively, in agreement with values reported in the literature.[86,87] On the other hand, Cu metal develops an unambiguous fingerprint that allows to identify traces of this material, although its L_3 absorption edge typically appears at around 933.5 eV, overlapping with the Cu_2O spectral features. Hence, herein we used the intensity ratios between the L_3 components with centers at ca. 930.7 and 933.7 eV as a qualitative indicator of the copper reduction degree and the results are compiled in Table 1. Comparing to XPS, NEXAFS analysis in total electron yield detection mode is sensitive

to deeper probing, estimated to be ca. 5 nm for semiconductors. [88]Altogether, these techniques provide a description of the copper oxidation state at different catalyst depths when complemented with XPS analysis. The combination of these techniques allows to infer that Cu reduction is partial in the bulk but complete at the outer surface of Cu particles, as evidenced from the data collected in Table 1.

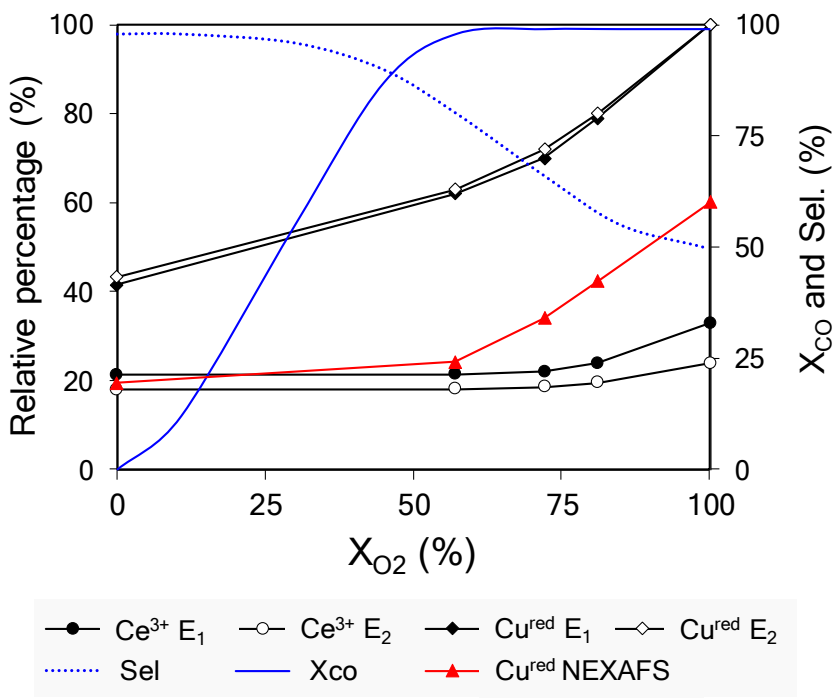

Figure 7. Main y-axis: Distribution of surface Ce^{3+} (circles) and reduced Cu species (i.e., Cu^{+} and Cu, diamonds) present in the CuO/CeO_2 catalyst during CO-PROX operando NAP–XPS experiment using 1082 eV (E_1, solid symbols); and 1372 eV (E_2, open

symbols) excitation energies. NEXAFS Cu species distribution (circles). Secondary y-axis: CO conversion (X_{CO}, solid line) and CO selectivity (*Sel,* dotted line) profiles

To correlate the XPS results with the CO-PROX catalytic activity, X_{O2} and X_{CO} were subsequently determined, which enabled the estimation of the CO selectivity along the temperature profile. Figure 7 shows the evolution of Ce^{3+} and reduced Cu species as determined by NAP–XPS and NEXAFS for the CuO/CeO_2 catalyst plotted as a function of X_{O2}. In short, gradual surface reduction of Cu species occurred along the CO-PROX reaction course, while only moderate and very superficial Ce reduction was observed from the ceria support at the maximum X_{O2}, where total X_{CO} is achieved along with the ongoing H_2 oxidation reaction. Our experiments also indicate that the presence of reduced copper is closely connected to H_2 oxidation reaction since it coincides with the observed CO selectivity decay, in line with previous studies.[17,54,89] In fact, because the surface Cu^+ abundance is extraordinarily high at the beginning of the CO-PROX reaction, CuO should be partially reduced on surface upon CO contact, resulting in a very anticipated (but limited) CO oxidation activity. As temperature increases, an enhancement

of the reaction rate is observed, which occurs via a MvK mechanism by means of lattice-O abstraction and eventually results in a gradual reduction of the Cu_xO particles, from the surface to the bulk. At the maximum measured temperature, however, with total X_{O2} and still maximum X_{CO}, no trace of CuO on the surface was detected and copper particles were found to exhibit Cu^0/Cu^+ mixed reduced states. Importantly, the Cu^0 content is likely to increase with temperature, which eventually will promote H_2 oxidation leading to more reduced Cu sites. In this scenario, it is expected that X_{CO} would decrease at higher temperatures at the expense of the boosted H_2 oxidation rate, besides an increasing inner (NEXAFS) Cu reduction degree. Unfortunately, the experimental settings of the NAP–XPS and NEXAFS analyses prevented us from further increasing the temperature beyond the value at which total X_{O2} was achieved.

As far as the catalyst support is concerned, the data presented in Table 1 indicate that CeO_2 remains oxidized in an equilibrium state until the CuO surface completely disappears. Furthermore, the differences observed between the results obtained at 1082 and 1372 eV excitation energies suggest that incipient ceria reduction is strictly limited to

the most superficial surface. CO-PROX operando NAP–XPS experiments also show that Ce^{3+} content remains constant while surface O_γ peak gradually grows up to a sharp increase at 450 ºC, which suggests that the potential hydroxylation does not have a significant impact on ceria reduction. Hence, we conclude that the lattice expansion observed in the CO-PROX-recorded Raman spectra up to 200 ºC (Figure 4b) is not due to the reduction of ceria. A plausible alternative explanation involves the reduction of copper species, particularly those Cu cations partially inserted into the ceria matrix upon the CuO loading, as revealed by XRD (Table S2). The reduction of inserted Cu^{2+} to Cu^{+} would implement a yet larger lattice expansion on ceria, besides a potential breaking up of the minor Cu-Ce solid solution stability. This effect is partially reversed between 100–200 ºC since ceria is expected to become more reduced as temperature increases at expenses of the labile redox equilibrium $Cu^{+} + Ce^{4+} \leftrightarrow Ce^{3+} + Cu^{2+}$, as H_2-TPR experiments show (Figure S4). However, in overall, Ce ions are likely to be in a steady oxidized redox state while Cu is reduced by the effect of CO-PROX reaction occurring via MvK mechanism and the imbalanced O abstraction–restorage equilibrium. Accordingly,

the lattice oxygen from the ceria support is performing an active role when CuO are entirely reduced on the surface, which is the point of total X_{O2} above which CO conversion drops. The mobilization of oxygen from CeO_2 at such stage might be assigned to the O transfer within the Cu–Ce interfaces, aiming to palliate the O-deficiency in the reduced Cu sites. Furthermore, the activation of the mobile interfacial oxygen at that low partial O_2 pressure could be related with the sharp increase seen at 450 ºC for the O_γ peak. Therefore, when X_{O2} is critically low, CeO_2 should aid the oxygen vacancy filling process over the active Cu species in a synergistic mechanism, either in complement or in replacement of the direct O_2 uptake on Cu.

3.6. Density functional theory calculations

The experimental data presented above suggest that O-vacancy sites are generated in CuO at temperatures within the selective CO-PROX regime (Region 1, Figure 1), while lattice O atoms in CeO_2 are involved at higher temperatures within the non-selective regime (Region 2, Figure 1). With the aim to shed light on this critical step, DFT+U calculations were conducted on different surface slabs that represent the most abundant

facets present in the CuO/CeO_2 catalyst. TEM characterization (Figure S5) allowed to elucidate the particle morphology in the heterogeneous CuO/CeO_2 catalyst, which exhibits a polycrystalline nature with irregular sizes and shapes. Accordingly, the preferential exposed facet in CeO_2 phase is {111}, that is the most stable surface for CeO_2,[90] while CuO presents too low contrast to discern the lattice spacing. In agreement with TEM analysis, the surface slabs modelled by DFT correspond to CeO_2(111), CuO(111) and Cu_2O(111), which are the most representative surfaces for each phase (Figure 8).[91]

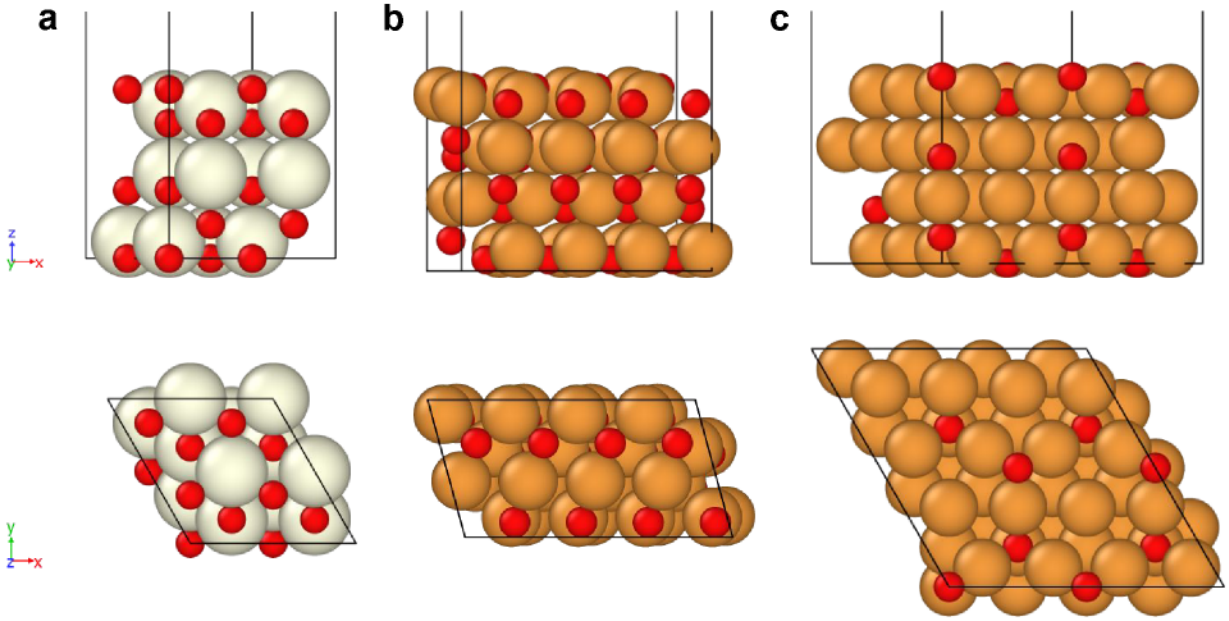

Figure 8. Side (above) and top (below) views of the DFT-modelled surface slabs: a) CeO_2(111) surface with 12 Ce (pale yellow) and 24 O (red) ions; b) CuO(111) surface with 32 Cu (brown) and 32 O ions; and c) Cu_2O(111) surface with 64 Cu and 32 O ions.

Because the reoxidation of a given oxide material is directly linked to its oxygen storage/release capacity, the energy required to create an O vacancy can be taken as a good reaction descriptor for that process. Thus, we set out to compute the oxygen vacancy formation energy ($E_{O\text{-}vac}$) for each of the surface slabs shown in Figure 8. Importantly, upon removal of an O atom, two electrons are left behind leading to the reduction of two Ce^{4+} ions to Ce^{3+}. The localization of the excess of electrons on the oxide surface has been extensively studied for CeO_2[49,66,92] showing that it can have a considerable effect on the calculated $E_{O\text{-}vac}$ value. Consequently, different electron localizations were considered upon the generation of an O vacancy on the various surface slabs (Table S4). The lowest energy configurations and electron localizations are shown in Table 2.

Table 2. O vacancy formation energies ($E_{O\text{-}vac}$, in eV) and localization of the excess of electrons for the CeO_2(111), CuO(111), and Cu_2O(111) surface slabs. *NN* and *NNN* denote nearest neighbor and next nearest neighbor, respectively.

	CeO_2(111)	CuO(111)	Cu_2O(111)
$E_{O\text{-}vac}$	2.22	2.34	1.97
e^- localization	*NN* / *NNN*	*NN* / 2*(*NN*/2)	delocalized

The energies included in Table 2 are in very good agreement with previous theoretical studies, although they are highly dependent on the localization of the two electrons left upon O abstraction.[66,92–94] These values correspond to the lowest O-vacancy formation energies calculated for the different phases and follow the trend: CuO(111) > CeO_2(111) > Cu_2O(111). Hence, the calculated data indicate that the formation of oxygen vacancies in CuO is thermodynamically less favored compared to CeO_2 despite experiments show a gradual CuO reduction and steady CeO_2 redox state for the CuO/CeO_2 catalyst during CO-PROX. The fact that CuO reduction prevails over CeO_2 reduction in the wide range

of the low-temperature CO selective regime is due to the different surface interaction in the presence of reducing gases from the gas stream (e.g. CO and H_2), which is not considered in the calculated $E_{O\text{-}vac}$ values as these only account for the oxygen abstraction from the surface to the gas phase. Nevertheless, it is evident that the higher the energy for the oxygen vacancy formation, the more facile lattice oxygen restorage when the O-deficient slabs are set in contact with O_2 atmosphere. Therefore, attending to the observed trend we can conclude that direct O-lattice regeneration should prevail in CuO when present, while the reoxidation through CeO_2 becomes more favorable once CuO is reduced to Cu_2O.

Altogether, DFT+*U* calculations predict a change in the reoxidation mechanism of CuO/CeO_2 catalyst that enhances Cu^+ stability during CO-PROX reaction course, which is summarized in Figure 9. At low temperature (Figures 9a-b), CuO particles are reduced and oxidized in imbalance equilibria where CO takes lattice oxygen and vacancies are replenished afterwards by O_2 from the gas feeding (i.e., direct mechanism). In this regime, the CuO_x particles solely undertake the whole cyclic reaction-oxidation processes

bypassing the participation via CeO_2. However, since ceria is closely interacting within the active Cu–[O_x]–Ce interfacial species, the surrounding CeO_2 matrix undergoes dynamic processes of lattice expansion which are not related to Ce redox changes, as well as the accumulation of surface intermediates. At higher temperatures (Figures 9c-d), CuO_x particles are reduced by H_2 in addition to CO, and the reduction/oxidation equilibrium shifts even more forwards reduction, which in turn hampers the thermodynamic O vacancy filling process. At such point, the tightly contacting CeO_2 phase is more prone to undertake O accommodation than the reduced Cu_2O/Cu species according to the computed O-binding strength. Subsequently, the transfer of surface O from CeO_2 to Cu_2O assists lattice O recovery in the reduced copper species at the triple-phase boundary, as evidenced in the lower X-ray energy test from NAP–XPS experiment (see Table 1).

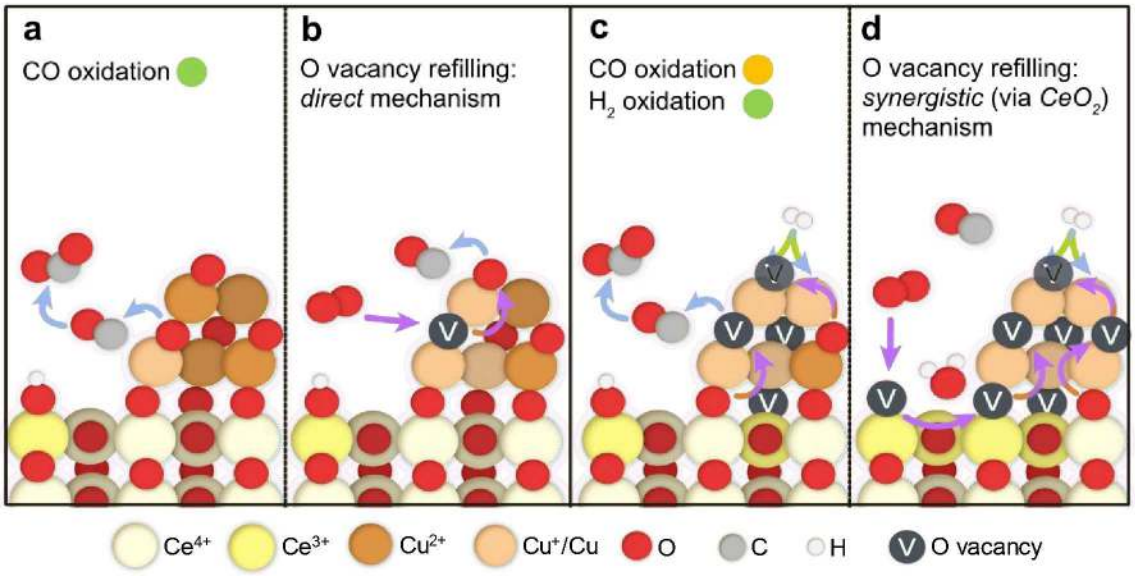

Figure 9. CO-PROX reaction scheme in CuO/CeO_2 catalyst in (a,b) the CO-selective regime, where CO oxidation prevails in the presence of Cu^+/CuO oxidized particles, and (c,d) in the non-CO selective regime, where H_2 oxidation domains over CO oxidation when copper species are reduced on surface to Cu/Cu_xO clusters. (a,c) display reaction schemes, creating O vacancies in the copper-rich phase while (b,d) refer to the subsequent O_2 uptake occurring in each regime.

The change from direct to synergistic reoxidation mechanism (via CeO_2) delays Cu particles reoxidation and CO conversion decays at expenses of H_2 oxidation. Overcoming such state leads to the gradual surface to bulk CeO_2 reduction that is observed in the in

situ Raman spectra as a very important growth on D band contribution. Catalytic tests (Figure 1) reveal that the excess of O_2 in $\lambda = 2$ conditions targets partially reduced copper particles, holding CO conversion in a certain extent within the Region 2, whereas in the stoichiometric conditions ($\lambda = 1$), reaching Region 2 means a straight decay in CO conversion. The enrolment of lattice oxygen from CeO_2 takes place mainly when copper particles are reduced on surface and present a significant partially reduced bulk state, too. Herein, the reduction of CeO_2 has been identified as a sign of CO selectivity loss, which should be related to the change in the reoxidation mechanism. This conclusion manifests that reoxidation issues should be contemplated in a CO-PROX reaction mechanism, where it is usually taken for granted regardless the O_2 partial pressures and temperature along the reaction run. Accordingly, results allow to conclude that the efficient O restorage may enhance the CO selectivity over conventional CuO/CeO_2 catalyst, which sheds some light in several decade-long debates. Namely, the controversy on the negative effect of ceria-doping in CO-PROX application, that restricts

Cu-Ce interaction, or the beneficial deployment of inverse CeO_2/CuO catalysts, with larger CuO particles and lowered reducibility.

4. Conclusions

This multidisciplinary study has combined an experimental and computational approach to tackle the CO-PROX reaction mechanism at the atomic scale over CuO/CeO_2 catalysts considering lattice oxygen recovery at play. First, the CO oxidation and H_2 oxidation reactions in CO-PROX conditions occur via Mars–van Krevelen mechanism along the entire range of reaction course with a gradual surface to bulk reduction of CuO particles. Increasing the partial pressure of O_2 is beneficial for the CO-PROX reaction since it maximizes the reactive surface oxygen up to the virtual limit imposed by the oxygen storage capacity of the CuO/CeO_2 catalyst, although H_2 oxidation onset is not affected. On the other hand, the surface of CeO_2 support is dynamic and experiences irregular lattice dilations upon the ongoing processes which are not related with Ce^{4+} reduction, but to the side-effect of present inserted Cu. The role of ceria is secondary while copper

particles remain partially oxidized, which undertake CO oxidation and H_2 oxidation reactions, besides their direct reoxidation with molecular O_2.

The reduction of CuO to Cu_2O/Cu^0 entails not only a further selectivity loss by the activation of H_2 oxidation, but also the stabilization of oxygen vacancies that hamper the thermodynamics of direct oxygen vacancy filling. With the presence of reduced Cu particles in the CuO/CeO_2 catalyst, the ceria support assists into the O uptake via a synergistic mechanism. At such point, surface reduction of CeO_2 is observed and when it is further extended, CO conversion drops in favor of H_2 oxidation. These results reveal that though CeO_2 reduction is detrimental to CO conversion, the improved surface reducibility of copper species plays a positive role. This knowledge will allow the rational catalyst design of the high-performance CuO/CeO_2 catalysts, and derived configurations, in pursuit of the optimum compromise in the tunable interfacial Cu–Ce redox properties.

AUTHOR INFORMATION

Corresponding Authors

Grupo de Materiales Carbonosos y Medio Ambiente (MCMA), Departamento de Química Inorgánica, Universidad de Alicante. Carretera San Vicente del Raspeig s/n E03080, Alicante (Spain). Tel. (+34) 965903538; E-mail: arantxa.davo@ua.es; agus@ua.es.

Present Address

[†]Carl Zeiss SMT GmbH, Rudolf-Eber-Straße. 2, 73447 Ober-kochen, Germany.

Author Contributions

The manuscript was written through contributions of all authors. All authors have given approval to the final version of the manuscript. All authors contributed equally to this work.

Supporting information.

Includes physicochemical characterization of the catalyst: N_2 adsorption at –196 ºC (Figure S1, Table S1), XRD (Figure S2, Table S2), Raman spectroscopy (Figure S3), temperature programmed reduction with H_2 (Figure S4) and transmission electron microscopy (Figure S5). Stability and durability tests under CO-PROX conditions (Figures S6-9), temperature programmed desorption (TPD) experiments (Figures S10a,b), global yield on isotopic experiments (Figure S11), CO-PROX operando DRIFTS (Figures

S12a,c), and additional data related to NAP–XPS (Table S3 and Figure S13) and DFT calculations (Figure S14).

The following files are available free of charge.

ACKNOWLEDGMENT

The authors thank the financial support of the Spanish Ministry of Economy and Competitiveness (Project CTQ2015-67597-C2-2-R and grant FJCI-2015-23769), the Spanish Ministry of Education, Culture and Sports (grant FPU14/01178), the Generalitat Valenciana (Project PROMETEO/2018/076) and the EU (FEDER funding). F.C.H. acknowledges the Argentinian National Research Council (CONICET) for the financial support. The authors thank the support of ALBA staff for the successful performance of the measurements at CIRCE beamline at the ALBA Synchrotron Light Source. The DJEI/DES/SFI/HEA Irish Centre for High-End Computing (ICHEC) is also acknowledged for the generous provision of computational facilities and support.

REFERENCES

(1) Farrauto, R.; Hwang, S.; Shore, L.; Ruettinger, W.; Lampert, J.; Giroux, T.; Liu, Y.; Ilinich, O. Generating Hydrogen for the PEM Fuel Cell. *Annu. Rev. Mater. Res.* **2003,** *33*, 1–27.

(2) Choudhary, T. V.; Goodman, D. W. CO-Free Fuel Processing for Fuel Cell Applications. *Catal. Today* **2002,** *77*, 65–78.

(3) Ghenciu, A. F. Review of Fuel Processing Catalysts for Hydrogen Production in PEM Fuel Cell Systems. *Curr. Opin. Solid State Mater. Sci.* **2002,** *6*, 389–399.

(4) Chen, C.-Y.; Huang, K.-P. Performance and Transient Behavior of the KW-Grade PEMFC Stack with the PtRu Catalyst under CO-Contained Diluted Hydrogen. *Int. J. Hydrogen Energy* **2017,** *42*, 22250–22258.

(5) Golunski, S. What Is the Point of On-Board Fuel Reforming? *Energy Environ. Sci.* **2010,** *3*, 1918–1923.

(6) Konsolakis, M. The Role of Copper–Ceria Interactions in Catalysis Science: Recent Theoretical and Experimental Advances. *Appl. Catal., B* **2016,** *198*, 49–66.

(7) Trovarelli, A. Catalytic Properties of Ceria and CeO_2-Containing Materials. *Catal. Rev.* **1996,** *38*, 439–520.

(8) Bueno-López, A. Diesel Soot Combustion Ceria Catalysts. *Appl. Catal., B* **2014,** *146*, 1–11.

(9) Park, E. D.; Lee, D.; Lee, H. C. Recent Progress in Selective CO Removal in a H_2-Rich Stream. *Catal. Today* **2009,** *139,* 280–290.

(10) Avgouropoulos, G.; Ioannides, T.; Matralis, H. Influence of the Preparation Method on the Performance of CuO-CeO_2 Catalysts for the Selective Oxidation of CO. *Appl. Catal., B* **2005,** *56*, 87–93.

(11) Martínez-Arias, A.; Gamarra, D.; Hungría, A.; Fernández-García, M.; Munuera, G.; Hornés, A.; Bera, P.; Conesa, J.; Cámara, A. Characterization of Active Sites/Entities and Redox/Catalytic Correlations in Copper-Ceria-Based Catalysts for Preferential Oxidation of CO in H_2-Rich Streams. *Catalysts* **2013,** *3*, 378–400.

(12) Martínez-Arias, A.; Fernández-García, M.; Soria, J.; Conesa, J. C. Spectroscopic Study of a Cu/CeO_2 Catalyst Subjected to Redox Treatments in Carbon Monoxide and Oxygen. *J. Catal.* **1999,** *182*, 367–377.

(13) Tang, X.; Zhang, B.; Li, Y.; Xu, Y.; Xin, Q.; Shen, W. CuO/CeO_2 Catalysts: Redox Features and Catalytic Behaviors. *Appl. Catal., A* **2005,** *288*, 116–125.

(14) Wang, C.; Cheng, Q.; Wang, X.; Ma, K.; Bai, X.; Tan, S.; Tian, Y.; Ding, T.; Zheng, L.; Zhang, J.; Li, X. Enhanced Catalytic Performance for CO Preferential Oxidation over CuO Catalysts Supported on Highly Defective CeO_2 Nanocrystals. *Appl. Surf. Sci.* **2017,** *422*, 932–943.

(15) Guo, X.; Qiu, Z.; Mao, J.; Zhou, R. Shape-Controlled $Cu_xCe_{1-x}O_2$ Nanorods Catalyst and the Active Components Functioned in Selective Oxidation of CO in Hydrogen-Rich Stream. *J. Power Sources* **2020,** *451*, 227757–227767.

(16) Martínez-Arias, A.; Hungría, A. B.; Munuera, G.; Gamarra, D. Preferential Oxidation of CO in Rich H_2 over CuO/CeO_2: Details of Selectivity and Deactivation under the Reactant Stream. *Appl. Catal., B* **2006,** *65*, 207–216.

(17) Polster, C. S.; Nair, H.; Baertsch, C. D. Study of Active Sites and Mechanism Responsible for Highly Selective CO Oxidation in H_2 Rich Atmospheres on a Mixed Cu and Ce Oxide Catalyst. *J. Catal.* **2009,** *266*, 308–319.

(18) Yang, L.; Zhou, S.; Ding, T.; Meng, M. Superior Catalytic Performance of Non-Stoichiometric Solid Solution $Ce_{1-x}Cu_xO_{2-\delta}$ Supported Copper Catalysts Used for CO Preferential Oxidation. *Fuel Process. Technol.* **2014,** *124*, 155–164.

(19) Gamarra, D.; Hornés, A.; Koppány, Z.; Schay, Z.; Munuera, G.; Soria, J.; Martínez-Arias, A. Catalytic Processes during Preferential Oxidation of CO in H_2-Rich Streams over Catalysts Based on Copper–Ceria. *J. Power Sources* **2007,** *169*, 110–116.

(20) Martínez-Arias, A.; Gamarra, D.; Fernández-García, M.; Hornés, A.; Belver, C. Spectroscopic Study on the Nature of Active Entities in Copper–Ceria CO-PROX Catalysts. *Top. Catal.* **2009,** *52*, 1425–1432.

(21) Monte, M.; Munuera, G.; Costa, D.; Conesa, J. C.; Martínez-Arias, A. Near-Ambient XPS Characterization of Interfacial Copper Species in Ceria-Supported Copper Catalysts. *Phys. Chem. Chem. Phys.* **2015,** *17*, 29995–30004.

(22) Qi, L.; Yu, Q.; Dai, Y.; Tang, C.; Liu, L.; Zhang, H.; Gao, F.; Dong, L.; Chen, Y. Influence of Cerium Precursors on the Structure and Reducibility of Mesoporous CuO-CeO_2 Catalysts for CO Oxidation. *Appl. Catal., B* **2012,** *119–120*, 308–320.

(23) Liu, W.; Flytzani-Stephanopoulos, M. Total Oxidation of Carbon-Monoxide and Methane over Transition Metal Fluorite Oxide Composite Catalysts. II. Catalyst Characterization and Reaction-Kinetics. *J. Catal.* **1995,** *153*, 317–332.

(24) Xu, C.; Li, S.; Zhang, Y.; Li, Y.; Zhou, J.; Qin, G. Synthesis of CuO_x–CeO_2 Catalyst with High-Density Interfaces for Selective Oxidation of CO in H_2-Rich Stream. *Int. J. Hydrogen Energy* **2019,** *44*, 4156–4166.

(25) Du, P.-P.; Wang, W.-W.; Jia, C.-J.; Song, Q.-S.; Huang, Y.-Y.; Si, R. Effect of Strongly Bound Copper Species in Copper–Ceria Catalyst for Preferential Oxidation of Carbon Monoxide. *Appl. Catal., A* **2016,** *518*, 87–101.

(26) Xie, Y.; Wu, J.; Jing, G.; Zhang, H.; Zeng, S.; Tian, X.; Zou, X.; Wen, J.; Su, H.; Zhong, C.-J.; Cui, P. Structural Origin of High Catalytic Activity for Preferential CO Oxidation over CuO/CeO_2 Nanocatalysts with Different Shapes. *Appl. Catal., B* **2018,** *239*, 665–676.

(27) Wang, W.-W.; Yu, W.-Z.; Du, P.-P.; Xu, H.; Jin, Z.; Si, R.; Ma, C.; Shi, S.; Jia, C.-J.; Yan, C.-H. Crystal Plane Effect of Ceria on Supported Copper Oxide Cluster Catalyst for CO Oxidation: Importance of Metal–Support Interaction. *ACS Catal.* **2017,** *7*, 1313–1329.

(28) Lykaki, M.; Pachatouridou, E.; Carabineiro, S. A. C.; Iliopoulou, E.; Andriopoulou, C.; Kallithrakas-Kontos, N.; Boghosian, S.; Konsolakis, M. Ceria Nanoparticles Shape Effects on the Structural Defects and Surface Chemistry: Implications in CO Oxidation by Cu/CeO_2 Catalysts. *Appl. Catal., B* **2018,** *230*, 18–28.

(29) Hornés, A.; Hungría, A. B.; Bera, P.; López Cámara, A.; Fernández-García, M.; Martínez-Arias, A.; Barrio, L.; Estrella, M.; Zhou, G.; Fonseca, J. J.; Hanson, J. C.; Rodriguez, J. A. Inverse CeO_2/CuO Catalyst as an Alternative to Classical Direct Configurations for Preferential Oxidation of CO in Hydrogen-Rich Stream. *J. Am. Chem. Soc.* **2010,** *132*, 34–35.

(30) Davó-Quiñonero, A.; Such-Basáñez, I.; Juan-Juan, J.; Lozano-Castelló, D.; Stelmachowski, P.; Grzybek, G.; Kotarba, A.; Bueno-López, A. New Insights into the Role of

Active Copper Species in CuO/Cryptomelane Catalysts for the CO-PROX Reaction. *Appl. Catal., B* **2020,** *267*, 118372–118383.

(31) Lu, J.; Wang, J.; Zou, Q.; He, D.; Zhang, L.; Xu, Z.; He, S.; Luo, Y. Unravelling the Nature of the Active Species as Well as the Doping Effect over Cu/Ce-Based Catalyst for Carbon Monoxide Preferential Oxidation. *ACS Catal.* **2019,** *9*, 2177–2195.

(32) Wang, F.; Büchel, R.; Savitsky, A.; Zalibera, M.; Widmann, D.; Pratsinis, S. E.; Lubitz, W.; Schüth, F. In Situ EPR Study of the Redox Properties of CuO–CeO_2 Catalysts for Preferential CO Oxidation (PROX). *ACS Catal.* **2016,** *6*, 3520–3530.

(33) Elias, J. S.; Stoerzinger, K. A.; Hong, W. T.; Risch, M.; Giordano, L.; Mansour, A. N.; Shao-Horn, Y. In Situ Spectroscopy and Mechanistic Insights into CO Oxidation on Transition-Metal-Substituted Ceria Nanoparticles. *ACS Catal.* **2017,** *7*, 6843–6857.

(34) Zhang, X.; House, S. D.; Tang, Y.; Nguyen, L.; Li, Y.; Opalade, A. A.; Yang, J. C.; Sun, Z.; Tao, F. F. Complete Oxidation of Methane on NiO Nanoclusters Supported on CeO_2 Nanorods through Synergistic Effect. *ACS Sustainable Chem. Eng.* **2018,** *6*, 6467–6477.

(35) Jia, A.-P.; Jiang, S.-Y.; Lu, J.-Q.; Luo, M.-F. Study of Catalytic Activity at the CuO−CeO_2 Interface for CO Oxidation. *J. Phys. Chem. C* **2010,** *114*, 21605–21610.

(36) Caputo, T.; Lisi, L.; Pirone, R.; Russo, G. On the Role of Redox Properties of CuO/CeO_2 Catalysts in the Preferential Oxidation of CO in H_2-Rich Gases. *Appl. Catal., A* **2008,** *348*, 42–53.

(37) Xia, Y.; Lao, J.; Ye, J.; Cheng, D.; Chen, F.; Zhan, X. Role of Two-Electron Defects on the CeO_2 Surface in CO Preferential Oxidation over CuO/CeO_2 Catalysts. *ACS Sustainable Chem. Eng.* **2019,** *7*, 18421–18433.

(38) Moreno, M.; Bergamini, L.; Baronetti, G. T.; Laborde, M. A.; Mariño, F. J. Mechanism of CO Oxidation over CuO/CeO_2 Catalysts. *Int. J. Hydrogen Energy* **2010,** *35*, 5918–5924.

(39) Il'ichev, A. N.; Firsova, A. A.; Korchak, V. N. Mechanism of CO Oxidation in Excess H_2 over CuO/CeO_2 Catalysts: ESR and TPD Studies. *Kinet. Catal.* **2006,** *47*, 585–592.

(40) Shi, J. On the Synergetic Catalytic Effect in Heterogeneous Nanocomposite Catalysts. *Chem. Rev.* **2013,** *113*, 2139–2181.

(41) Pérez-Dieste, V.; Aballe, L.; Ferrer, S.; Nicolàs, J.; Escudero, C.; Milán, A.; Pellegrin, E. Near Ambient Pressure XPS at ALBA. *J. Phys.: Conf. Ser.* **2013,** *425*, 72023–72027.

(42) Perdew, J. P.; Burke, K.; Ernzerhof, M. Generalized Gradient Approximation Made Simple. *Phys. Rev. Lett.* **1996,** *77*, 3865–3868.

(43) Kresse, G.; Furthmüller, J. Efficiency of Ab-Initio Total Energy Calculations for Metals and Semiconductors Using a Plane-Wave Basis Set. *Comput. Mater. Sci.* **1996,** *6*, 15–50.

(44) Kresse, G.; Furthmüller, J. Efficient Iterative Schemes for Ab Initio Total-Energy Calculations Using a Plane-Wave Basis Set. *Phys. Rev. B* **1996,** *54*, 11169–11186.

(45) Blöchl, P. E. Projector Augmented-Wave Method. *Phys. Rev. B* **1994,** *50*, 17953–17979.

(46) Dudarev, S. L.; Botton, G. A.; Savrasov, S. Y.; Humphreys, C. J.; Sutton, A. P. Electron-Energy-Loss Spectra and the Structural Stability of Nickel Oxide: An LSDA+U Study. *Phys. Rev. B* **1998,** *57*, 1505–1509.

(47) Fabris, S.; de Gironcoli, S.; Baroni, S.; Vicario, G.; Balducci, G. Taming Multiple Valency with Density Functionals: A Case Study of Defective Ceria. *Phys. Rev. B* **2005,** *71*, 41102–41106.

(48) Nolan, M.; Grigoleit, S.; Sayle, D. C.; Parker, S. C.; Watson, G. W. Density Functional Theory Studies of the Structure and Electronic Structure of Pure and Defective Low Index Surfaces of Ceria. *Surf. Sci.* **2005,** *576*, 217–229.

(49) García-Melchor, M.; López, N. Homolytic Products from Heterolytic Paths in H_2 Dissociation on Metal Oxides: The Example of CeO_2. *J. Phys. Chem. C* **2014,** *118*, 10921–10926.

(50) García-Melchor, M.; Bellarosa, L.; López, N. Correction to Unique Reaction Path in Heterogeneous Catalysis: The Concerted Semi-Hydrogenation of Propyne to Propene on CeO_2. *ACS Catal.* **2015,** *5*, 1525–1553.

(51) Maimaiti, Y.; Nolan, M.; Elliott, S. D. Reduction Mechanisms of the CuO(111) Surface through Surface Oxygen Vacancy Formation and Hydrogen Adsorption. *Phys. Chem. Chem. Phys.* **2014,** *16*, 3036–3046.

(52) Davó-Quiñonero, A.; Navlani-García, M.; Lozano-Castelló, D.; Bueno-López, A.; Anderson, J. A. Role of Hydroxyl Groups in the Preferential Oxidation of CO over Copper Oxide-Cerium Oxide Catalysts. *ACS Catal.* **2016,** *6*, 1723–1731.

(53) Avgouropoulos, G.; Ioannides, T.; Matralis, H. K.; Batista, J.; Hocevar, S. CuO–CeO_2 Mixed Oxide Catalysts for the Selective Oxidation of Carbon Monoxide in Excess Hydrogen. *Catal. Lett.* **2001,** *73*, 33–40.

(54) Gamarra, D.; Munuera, G.; Hungria, A. B.; Fernandez-Garcia, M.; Conesa, J. C.; Midgley, P. A.; Wang, X. Q.; Hanson, J. C.; Rodriguez, J. A.; Martinez-Arias, A. Structure-Activity Relationship in Nanostructured Copper-Ceria-Based Preferential CO Oxidation Catalysts. *J. Phys. Chem. C* **2007,** *111*, 11026–11038.

(55) Kahlich, M. J.; Gasteiger, H. A.; Behm, R. J. Kinetics of the Selective Low-Temperature Oxidation of CO in H_2-Rich Gas over Au/α-Fe_2O_3. *J. Catal.* **1999,** *182*, 430–440.

(56) Mariño, F.; Descorme, C.; Duprez, D. Noble Metal Catalysts for the Preferential Oxidation of Carbon Monoxide in the Presence of Hydrogen (PROX). *Appl. Catal., B* **2004,** *54*, 59–66.

(57) Lee, H. C.; Kim, D. H. Kinetics of CO and H_2 Oxidation over CuO-CeO_2 Catalyst in H_2 Mixtures with CO_2 and H_2O. *Catal. Today* **2008,** *132*, 109–116.

(58) Zhang, R.; Miller, J. T.; Baertsch, C. D. Identifying the Active Redox Oxygen Sites in a Mixed Cu and Ce Oxide Catalyst by in Situ X-Ray Absorption Spectroscopy and Anaerobic Reactions with CO in Concentrated H_2. *J. Catal.* **2012,** *294*, 69–78.

(59) Jia, A. P.; Hu, G. S.; Meng, L.; Xie, Y. L.; Lu, J. Q.; Luo, M. F. CO Oxidation over CuO/$Ce_{1-x}Cu_xO_{2-\delta}$ and $Ce_{1-x}Cu_xO_{2-\delta}$ Catalysts: Synergetic Effects and Kinetic Study. *J. Catal.* **2012,** *289*, 199–209.

(60) Gamarra, D.; Martínez-Arias, A. Preferential Oxidation of CO in Rich H_2 over CuO/CeO_2: Operando-DRIFTS Analysis of Deactivating Effect of CO_2 and H_2O. *J. Catal.* **2009,** *263*, 189–195.

(61) Guo, M.; Lu, J.; Wu, Y.; Wang, Y.; Luo, M. UV and Visible Raman Studies of Oxygen Vacancies in Rare-Earth-Doped Ceria. *Langmuir* **2011,** *27*, 3872–3877.

(62) McBride, J. R.; Hass, K. C.; Poindexter, B. D.; Weber, W. H. Raman and X-ray Studies of $Ce_{1-x}RE_xO_{2-y}$, Where RE=La, Pr, Nd, Eu, Gd, and Tb. *J. Appl. Phys.* **1994,** *76*, 2435–2441.

(63) Taniguchi, T.; Watanabe, T.; Sugiyama, N.; Subramani, A. K.; Wagata, H.; Matsushita, N.; Yoshimura, M. Identifying Defects in Ceria-Based Nanocrystals by UV Resonance Raman Spectroscopy. *J. Phys. Chem. C* **2009,** *113*, 19789–19793.

(64) Xu, Y.; Wang, F.; Liu, X.; Liu, Y.; Luo, M.; Teng, B.; Fan, M.; Liu, X. Resolving a Decade-Long Question of Oxygen Defects in Raman Spectra of Ceria-Based Catalysts at Atomic Level. *J. Phys. Chem. C* **2019,** *123*, 18889–18894.

(65) Nakajima, A.; Yoshihara, A.; Ishigame, M. Defect-Induced Raman Spectra in Doped CeO_2. *Phys. Rev. B* **1994,** *50*, 13297–13307.

(66) Ganduglia-Pirovano, M. V.; da Silva, J. L. F.; Sauer, J. Density-Functional Calculations of the Structure of Near-Surface Oxygen Vacancies and Electron Localization on CeO_2(111). *Phys. Rev. Lett.* **2009,** *102*, 26101–26105.

(67) Hamilton, J. C.; Farmer, J. C.; Anderson, R. J. In Situ Raman Spectroscopy of Anodic Films Formed on Copper and Silver in Sodium Hydroxide Solution. *J. Electrochem. Soc.* **1986,** *133*, 739–745.

(68) Pushkarev, V. v; Kovalchuk, V. I.; d'Itri, J. L. Probing Defect Sites on the CeO_2 Surface with Dioxygen. *J. Phys. Chem. B* **2004,** *108*, 5341–5348.

(69) Schilling, C.; Hofmann, A.; Hess, C.; Ganduglia-Pirovano, M. V. Raman Spectra of Polycrystalline CeO_2: A Density Functional Theory Study. *J. Phys. Chem. C* **2017,** *121*, 20834–20849.

(70) Bernal, S.; Calvino, J. J.; Cifredo, G. A.; Rodriguez-Izquierdo, J. M. Comments on "Redox Processes on Pure Ceria and Rh/CeO_2 Catalyst Monitored by X-Ray Absorption (Fast Acquisition Mode). *J. Phys. Chem.* **1995,** *99*, 11794–11796.

(71) di Benedetto, A.; Landi, G.; Lisi, L. CO Reactive Adsorption at Low Temperature over CuO/CeO_2 Structured Catalytic Monolith. *Int. J. Hydrogen Energy* **2017,** *42*, 12262–12275.

(72) Tanuma, S.; Powell, C.J.; Penn, D.R. Calculations of electron inelastic mean free paths. V. Data for 14 organic compounds over the 50–2000 eV range. *Surf. Interface Anal.* **1994,** *21*, 165–176; calculated using QUASES-IMFP-TPP2M software, version 3.0; Tougaard, S., 2016.

(73) Jablonski, A. Quantification of Surface-Sensitive Electron Spectroscopies. *Surf. Sci.* **2009,** *603*, 1342–1352.

(74) Powell, C. J.; Jablonski, A. Evaluation of Calculated and Measured Electron Inelastic Mean Free Paths Near Solid Surfaces. *J. Phys. Chem. Ref. Data* **1999,** *28*, 19–62.

(75) Krawczyk, M.; Holdynski, M.; Lisowski, W.; Sobczak, J. W.; Jablonski, A. Electron Inelastic Mean Free Paths in Cerium Dioxide. *Appl. Surf. Sci.* **2015,** *341*, 196–202.

(76) Burroughs, P.; Hamnett, A.; Orchard, A. F.; Thornton, G. Satellite Structure in the X-Ray Photoelectron Spectra of Some Binary and Mixed Oxides of Lanthanum and Cerium. *J. Chem. Soc., Dalton Trans.* **1976,** 17, 1686–1698.

(77) Romeo, M.; Bak, K.; el Fallah, J.; le Normand, F.; Hilaire, L. XPS Study of the Reduction of Cerium Dioxide. *Surf. Interface Anal.* **1993,** *20*, 508–512.

(78) Praline, G.; Koel, B. E.; Hance, R. L.; Lee, H.-I.; White, J. M. X-Ray Photoelectron Study of the Reaction of Oxygen with Cerium. *J. Electron Spectrosc. Relat. Phenom.* **1980,** *21*, 17–30.

(79) Deshpande, S.; Patil, S.; Kuchibhatla, S. V. N. T.; Seal, S. Size Dependency Variation in Lattice Parameter and Valency States in Nanocrystalline Cerium Oxide. *Appl. Phys. Lett.* **2005,** *87*, 133113–133117.

(80) Poulston, S.; Parlett, P. M.; Stone, P.; Bowker, M. Surface Oxidation and Reduction of CuO and Cu_2O Studied Using XPS and XAES. *Surf. Interface Anal.* **1996,** *24*, 811–820.

(81) Salvador, P.; Fierro, J. L. G.; Amador, J.; Cascales, C.; Rasines, I. XPS Study of the Dependence on Stoichiometry and Interaction with Water of Copper and Oxygen Valence States in the $YBa_2Cu_3O_{7-x}$ Compound. *J. Solid State Chem.* **1989,** *81*, 240–249.

(82) Biesinger, M. C. Advanced Analysis of Copper X-Ray Photoelectron Spectra. *Surf. Interface Anal.* **2017,** *49*, 1325–1334.

(83) Biesinger, M. C.; Payne, B. P.; Hart, B. R.; Grosvenor, a P.; McIntryre, N. S.; Lau, L. W.; Smart, R. S. Quantitative Chemical State XPS Analysis of First Row Transition Metals, Oxides and Hydroxides. *J. Phys.: Conf. Ser.* **2008,** *100*, 12025–12029.

(84) Sarangi, R.; Aboelella, N.; Fujisawa, K.; Tolman, W. B.; Hedman, B.; Hodgson, K. O.; Solomon, E. I. X-Ray Absorption Edge Spectroscopy and Computational Studies on $LCuO_2$ Species: Superoxide−CuII versus Peroxide−CuIII Bonding. *J. Am. Chem. Soc.* **2006,** *128*, 8286–8296.

(85) George, S. J.; Lowery, M. D.; Solomon, E. I.; Cramer, S. P. Copper L-Edge Spectral Studies: A Direct Experimental Probe of the Ground-State Covalency in the Blue Copper Site in Plastocyanin. *J. Am. Chem. Soc.* **1993,** *115*, 2968–2969.

(86) Jiang, P.; Prendergast, D.; Borondics, F.; Porsgaard, S.; Giovanetti, L.; Pach, E.; Newberg, J.; Bluhm, H.; Besenbacher, F.; Salmeron, M. Experimental and Theoretical Investigation of the Electronic Structure of Cu_2O and CuO Thin Films on Cu(110) Using X-Ray Photoelectron and Absorption Spectroscopy. *J. Chem. Phys.* **2013,** *138*, 24704–24710.

(87) Shimizu, K.; Maeshima, H.; Yoshida, H.; Satsuma, A.; Hattori, T. Deconvolution Analysis of Cu L-Edge XANES for Quantification of Copper (II) Coordinations in Copper-Aluminate Catalysts. *Jpn. J. Appl. Phys.* **1999,** *38*, 44–48.

(88) Hähner, G. Near edge X-ray absorption fine structure spectroscopy as a tool to probe electronic and structural properties of thin organic films and liquids. *Chem. Soc. Rev.* **2006,** *35*, 1244–1255.

(89) Gamarra, D.; Cámara, A. L.; Monte, M.; Rasmussen, S. B.; Chinchilla, L. E.; Hungría, A. B.; Munuera, G.; Gyorffy, N.; Schay, Z.; Corberán, V. C.; Conesa, J. C.; Martínez-Arias, A. Preferential Oxidation of CO in Excess H_2 over CuO/CeO_2 Catalysts: Characterization and Performance as a Function of the Exposed Face Present in the CeO_2 Support. *Appl. Catal., B* **2013,** *130–131*, 224–238.

(90) Baudin, M.; Wójcik, M.; Hermansson, K. Dynamics, Structure and Energetics of the (111), (011) and (001) Surfaces of Ceria. *Surf. Sci.* **2000,** *468*, 51–61.

(91) Soon, A.; Todorova, M.; Delley, B.; Stampfl, C. Thermodynamic Stability and Structure of Copper Oxide Surfaces: A First-Principles Investigation. *Phys. Rev. B* **2007,** *75*, 125420–125429.

(92) Nolan, M.; Fearon, J. E.; Watson, G. W. Oxygen Vacancy Formation and Migration in Ceria. *Solid State Ionics* **2006,** *177*, 3069–3074.

(93) Nolan, M.; Elliott, S. D. The P-Type Conduction Mechanism in Cu_2O: A First Principles Study. *Phys. Chem. Chem. Phys.* **2006,** *8*, 5350–5358.

(94) Korzhavyi, P. A.; Johansson, B. *Literature Review on the Properties of Cuprous Oxide Cu_2O and the Process of Copper Oxidation*; Technical Report TR-11-08; Swedish Nuclear Fuel and Waste Management: Sweden, 2011.

Abstract graphic